Assessing Pt and Ni dissolution mechanism and kinetics of shape-controlled oxygen reduction nanocatalysts

Camille Roiron, Vincent Martin, Kavita Kumar, Laetitia Dubau, Frédéric Maillard

Assessing Pt and Ni dissolution mechanism and kinetics of shape-controlled oxygen reduction nanocatalysts

Camille Roiron [1,⊥], Vincent Martin [1,⊥], Kavita Kumar [1], Laetitia Dubau [1,], Frédéric Maillard [1,*]*

[1] Univ. Grenoble Alpes, Univ. Savoie Mont Blanc, CNRS, Grenoble INP$^{\Psi}$, LEPMI, 38000 Grenoble, France.

[⊥] These authors contributed equally to this work.

* Corresponding authors.

* L.D. Tel: +33 476 826 592. E-mail: laetitia.dubau@grenoble-inp.fr

* F.M. Tel: +33 476 826 592. E-mail: frederic.maillard@grenoble-inp.fr

ABSTRACT

An electrochemical flow cell combined with inductively coupled plasma mass spectrometry (FC-ICP-MS) is a powerful tool to understand the mechanisms of metal dissolution and to develop mitigation strategies. Herein, we quantified *in situ* the amount of Pt and Ni atoms dissolved from PtNi/C nanocatalysts employed to electrocatalyze the oxygen reduction reaction (ORR) in proton-exchange membrane fuel cell cathode. The nanocatalysts feature similar crystallite size and Pt:Ni atomic ratio but different morphologies (spheres, octahedra, sponges). The FC-ICP-MS results reveal that the nanocatalyst morphology affects the dissolution rate of Pt and Ni but not the dissolution mechanism. We provide analytical evidence that dissolution of Pt atoms is consistently accompanied by the dissolution of Ni atoms exceeding the stoichiometric composition. Furthermore, we demonstrate that *ex situ* acid leaching mitigates, but does not entirely prevent, the electrochemical dissolution of Ni atoms. Stabilized Pt and Ni dissolution rates were achieved after a one hour long accelerated stress test (AST). Characterization cyclic voltammograms show that the Pt dissolution rate remains constant before and after the AST. In contrast, the dissolution rate of Ni decreases by a factor of 10 after the AST. Among various nanoparticle shapes, spherical PtNi/C nanoparticles offer the best solution regarding the Pt and Ni retention compared to other nanoparticle shapes.

Keywords: Shape-controlled PtNi nanocatalysts; Degradation mechanisms; Oxygen reduction reaction; Durability; Electrochemical flow cell combined with inductively-coupled plasma mass spectrometry;

INTRODUCTION

Understanding and controlling the electrochemical stability of nanocatalyst is crucial for a wide range of applications, including proton-exchange membrane fuel cells (PEMFCs). In these devices, the oxygen reduction reaction (ORR) takes place at the cathode and the hydrogen oxidation reaction (HOR) at the anode. The acidic environment of a PEMFC lays constraints on the choice of catalytic materials, and both reactions are catalyzed by platinum (Pt)-based nanoparticles deposited on high-surface area carbon black. As Pt is a scarce and expensive metal, researchers work to reduce its content. Due to the five-order-of-magnitude slower kinetics of ORR on Pt compared to that of HOR, 80-90 % of Pt is placed at the cathode [1]. Reducing the Pt content at the cathode of PEMFCs can thus offer both economic and environmental advantages. The first approach to reduce the Pt content in PEMFCs entails the synthesis of electrocatalytically more active PtM/C nanocatalysts (where M is a transition metal). Combining Pt with early (*e.g.* Sc, Tb, Gd, Pr or Y) or late (*e.g*. Co, Ni, Cu or Cr) transition metals [2-6] is currently considered the best approach to reach high mass activity (MA, the current produced per gram of Pt) values. Indeed, not only do Pt-based alloys contribute to a direct reduction of the Pt mass, but they also substantially enhance the ORR kinetics via strain and ligand effects, both weakening the binding energy to the ORR intermediates [2, 7-9]. Moreover, as the (111) is the most active crystallographic orientation for the ORR, [10, 11] further enhancement of the ORR kinetics is possible on Pt-transition metal alloys exposing exclusively (111) facets. Octahedral or truncated octahedral Pt-alloy/C nanoparticles with between 14 and 21-fold increase of the specific activity (electrocatalytic activity per unit surface area of Pt) for the ORR *vs*. Pt/C in liquid electrolyte have been synthesized [12, 13]. The gain of shape-controlled Pt-alloy nanostructures *vs*. Pt/C is consistently smaller in terms of MA with only 7 to 15-fold increase due to their larger size. Defect-engineered catalysts, such as hollow PtNi/C nanoparticles, porous PtNi/C nanoparticles or self-standing PtNi aerogels, is another class of promising ORR catalysts [13-21]. In contrast to shape-controlled Pt-alloy, where catalytic sites are uniform and synthetically controlled to achieve optimal binding energy of the ORR intermediates, enhanced ORR kinetics of defective Pt-alloy nanocatalysts arises from the wide variety of catalytic sites' configurations present at their surface [13, 22]. On defective Pt-alloy catalysts, each site exhibits distinct structural and electronic

characteristics. Some of these sites demonstrate optimal binding to the ORR intermediates, thereby reaching the apex of the so-called volcano plot correlating ORR activity with the binding energy to key ORR intermediates. A 9.3- and a 5.8-fold enhancement of the ORR specific and mass activity at 0.95 V *vs*. Pt/C were achieved by a porous PtNi/C catalyst. (Sponge PtNi/C) [13, 23]. The record for this class of materials is a 33-fold enhancement of the ORR specific activity at 0.90 V *vs.* Pt/C on jagged Pt nanowires formed by complete dealloying of PtNi nanowires [16].

Now, the durability of the two classes of materials (shape-controlled/structurally-ordered *vs.* structurally-disordered), *i.e*., their capacity to maintain a constant ORR mass activity in the operating conditions of a PEMFC cathode, remains underexplored. It is well-documented from studies with rotating disk electrode (RDE) set-up [24-29] or in PEMFC devices [30-35] that transition metal atoms are leached out from the outermost 2-3 surface layers during operation, leading to the formation of a so-called 'Pt-skeleton' structure in which a Pt-rich shell covers the mother Pt-alloy core [29, 36]. Further dissolution of the alloying element results in relaxation (expansion) of the lattice parameter of Pt surface atoms, diminishing their ORR activity [30-32, 34]. Besides, shape-controlled Pt-alloy structures tend to return to their thermodynamically stable equilibrium shape during PEMFC operation, gradually losing their catalytic advantage over spherical particles [12, 13]. For example, we reported a 62 % loss of ORR specific activity after 20,000 potential cycles between 0.6 and 1.0 V for an octahedral PtNi/C (note that the loss was already 50 % after 2 consecutive ORR polarization curves), which we ascribed to the combined effects of structural reorganization and Ni leaching [13]. In contrast, on a structurally-disordered catalyst (Sponge PtNi/C), the ORR specific activity dropped by 13 % after 2 consecutive ORR polarization curves and by 34 % after 20 k potential cycles.

Better understanding of the dissolution mechanisms of Pt/C and Pt -alloy/C nanocatalysts was achieved in the last decade using an electrochemical flow cell connected to inductively coupled mass spectrometry (FC-ICP-MS) [37-42]. A FC-ICP-MS setup provides a time- and potential-resolved concentration profile of the metal atoms dissolved in the electrolyte, which can then be correlated with various operational parameters (pH, temperature, nature of the electrolyte) [43-47]. In particular, it has been shown that Pt is dissolved in two distinct phases: the anodic Pt dissolution takes place during the

formation of surface oxides, and the cathodic dissolution during their reduction [43, 44]. These findings are in line with the 'place-exchange' process, in which Pt and oxygen atoms swap their place at high electrode potential. The place-exchange concept was first introduced in surface science by Lanyon *et al*. to explain the oxidation kinetics of transition metals in an oxygen atmosphere at 138 °C, [48] and then subsequently adapted to electrochemistry [49, 50]. Using electrochemical quartz crystal microbalance and X-ray scattering, Nagy and Jerkiewicz showed that the place-exchange process occurs at potentials higher than 0.9 V/1.1 V on polycrystalline Pt and Pt(111), respectively [51, 52]. However, this "critical" potential also depends on parameters such as the crystallographic orientation, the crystallite size, the temperature, the pH, and the nature of the anions in the electrolyte [39, 43, 45, 53]. Using *in situ* high-energy surface X-ray diffraction, *in situ* inductively coupled plasma mass spectrometry and density functional theory calculations, Fuchs *et al*. [54] recently reported that the rate of Pt dissolution is much higher at Pt(100) than at Pt(111) surfaces. They related these differences to different oxophilicity of the two single crystal surfaces (Pt was shown to be 'extracted' (dissolved) above 0.98 V and 1.06 V on Pt(100) and Pt(111), respectively). Recently, the same authors evidenced the formation of two distinct oxide phases on Pt(100): an internal stripe-like oxide and an outer amorphous Pt oxide phase, which initiates its growth once the coverage of the stripe-like oxide reaches saturation [55]. They related these two oxides phases to anodic and cathodic Pt dissolution, respectively. On Pt/C nanoparticles, little to no Pt dissolution was measured using FC-ICP-MS set-up when the electrode potential remains inferior to 0.85 V [39, 40, 43-45, 53] but excursions to higher electrode potentials were shown to promote the cathodic Pt dissolution [44]. Transient conditions were shown to amplify the extent of Pt dissolution when compared to steady-state conditions [43, 56]. The electrolyte temperature also plays a crucial role. Cherevko *et al*. [53] showed that an increase in temperature leads to a higher dissolution of Pt during oxide formation, while the dissolution kinetics of Pt during oxide reduction decreases with rising temperature (a polycrystalline Pt foil was used by the authors). These results were nicely complemented by Đukić *et al*. [57] who showed that the redeposition of Pt cations is facilitated at higher temperature. Hence, changes in size and morphology occurring on n fuel cell catalysts are well reproduced when ASTs conducted in laboratories are carried out at 80°C rather than at temperature close to ambient, as first highlighted by Dubau *et al*. [58]. On Pt-alloys, the FC-ICP-MS results from Cherevko *et al*., Hodnik

et al. and Myers *et al*. suggested that Pt and the alloying element dissolve simultaneously during anodic sweeps, while Pt dissolution consistently precedes the dissolution of the alloying element during cathodic sweeps [40, 57, 59-61]. Đukić *et al*. [57, 61] also reported that the amount of dissolved Pt and alloying element increases with increasing the upper potential limit (UPL). In contrast, decreasing the lower potential limit (LPL) below 0.70 V proved to intensify the dissolution of the alloying element while lowering the Pt concentration in solution due to electrochemical redeposition of Pt^{z+} (z = 2, 4) cations. The above studies therefore laid the ground for elucidating the relationship between the chemical composition and the rate of dissolution of both Pt and the alloying element. However, so far, the effect of nanoparticle shape on the resistance to dissolution of both Pt and Ni has not been explored, and it is not clear which family of PtNi/C nanocatalysts (octahedral spongy or spherical nanoparticles) is most durable in the hash operating conditions of a PEMFC cathode.

To address this important issue, we herein synthesized two in-house PtNi/C catalysts with octahedral and 'sea sponge' nanoparticles, which we refer to as Octahedron PtNi/C and Sponge PtNi/C, respectively. For the sake of comparison, a commercial Pt_3Ni/C catalyst (Premetek®) and a commercial Pt/C catalyst (Heraeus®) with spherical nanoparticles were also used: these are referred to as Sphere PtNi/C and Sphere Pt/C, respectively. Using *in situ* FC-ICP-MS, we monitored the concentrations of the Pt and Ni dissolution signals during a 2-hour electrochemical aging protocol composed of multiple steps: break-in, characterization cyclic voltammograms (CVs) and accelerated stress test (AST). The effect of *ex situ* acid leaching on the extent of dissolution of Pt and Ni is also examined.

RESULTS AND DISCUSSION

1. Structural and chemical properties of the pristine Pt and PtNi electrocatalysts and description of the electrochemical aging protocol

Transmission electron microscopy (TEM) images of the as-synthesized catalysts are presented in **Figure 1a**. Their particle size distributions and chemical composition can be found in **Supplementary Figure 1** and **Supplementary Table 1**, respectively. Sphere PtNi/C is a commercial $Pt_{3.1}Ni$ catalyst produced by Premetek® with number-averaged mean particle size of 5.0 nm (see **Supporting**

Information). A commercial Pt/C catalyst of monodispersed size distribution (number-averaged diameter of 3.5 nm) produced by Heraeus® was used as a Ni-free reference (Sphere Pt/C). The Sponge PtNi/C catalyst is composed of *ca* 3 nm $Pt_{2.2}Ni$ crystallites aggregated into larger agglomerates *ca* 50 - 100 nm in size. The lattice of Sponge PtNi/C is defective due to its multi-grained structure and the presence of grain boundaries. Octahedral $Pt_{2.6}Ni$ nanoparticles with average length of 5.0 ± 0.7 nm were synthesized in a similar manner as in Ref. [62] (Octahedron PtNi/C). The high-energy X-ray diffractograms recorded on each material are shown in **Supplementary Figure 2**: they display a single alloyed crystalline phase for all PtNi/C materials and a single pure Pt phase for the Pt/C material. Note that all nanocatalysts were supported onto Vulcan XC72, a carbon black with specific surface area of *ca* 250 $m^2\ g^{-1}$. Moreover, all thin-film electrodes used in FC-ICP-MS experiments featured Pt loading comprised between 20 and 24 $\mu g_{Pt}\ cm^{-2}_{geo}$, translating into similar thickness. This is an important point given the influence of this parameter on the amount of Pt^{z+} cations released in the liquid electrolyte [40].

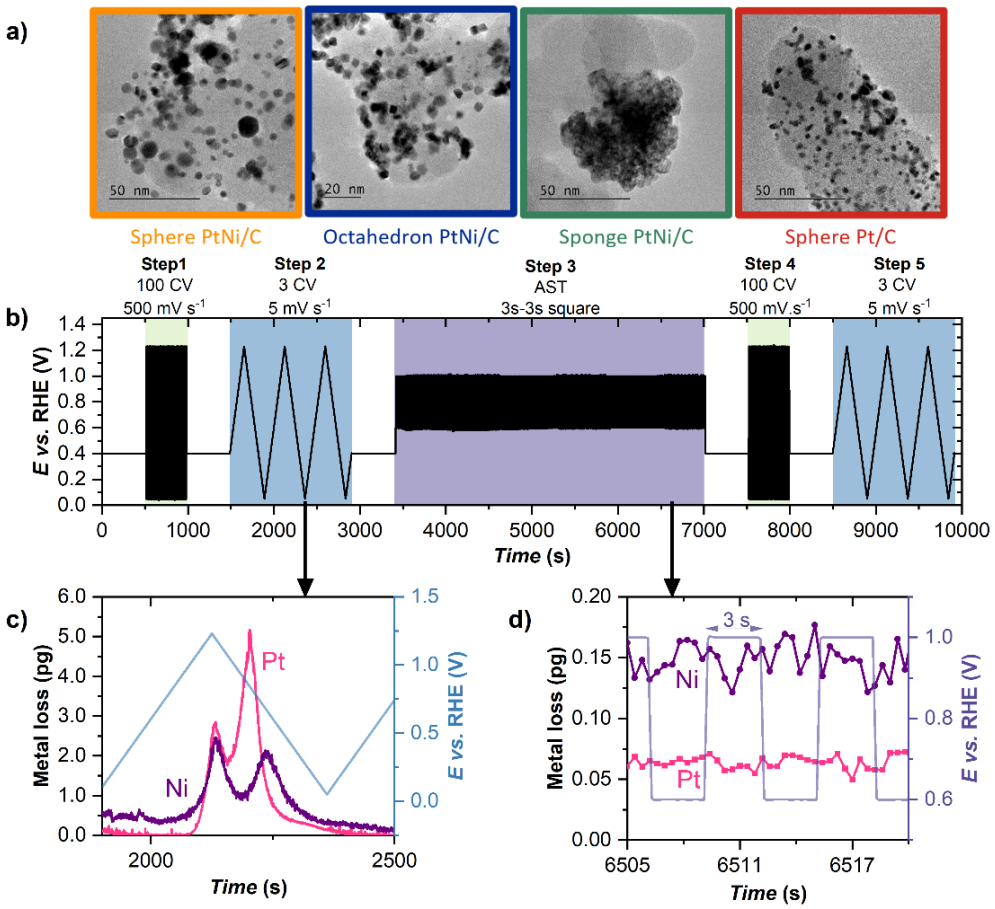

Figure 1. Experimental protocol used to investigate the dissolution of Pt and Ni from the different PtNi/C catalysts. a) TEM images of the various Pt/C and PtNi/C catalysts used in this study, b) electrochemical aging protocol, c) example of time-resolved dissolution of Pt and Ni during slow CV (5 mV s^{-1}) for the Sponge PtNi/C catalyst, d) zoom in on the dissolution of Pt and Ni during the AST for the Sponge PtNi/C catalyst.

Figure 1b illustrates the electrochemical aging protocol used in this study. A break-in procedure composed of 100 potential cycles between 0.05 V and 1.23 V at 500 mV s^{-1} was first conducted (Step 1). In line with our recent study on the conditioning of Pt-alloy catalysts, [63] an UPL of 1.23 V was chosen to achieve a stabilized surface state. It is clear from **Supplementary Figure 3**, the Pt dissolution signal stabilizes much more rapidly than the Ni dissolution signal. On Octahedron PtNi/C, for instance; the Pt dissolution signal attains an optimum after 11 seconds and stabilizes at *ca*. 3.0 x 10^{-4} ng_{Pt} cm^{-2}_{Pt} after 80 seconds. In contrast, the Ni dissolution signal reaches its optimum after 60 seconds and remains at a high level (> 2.7 x 10^{-2} ng_{Ni} cm^{-2}_{Pt}) during the whole break-in procedure. This outcome is the result of two phenomena: the preferential dissolution of low-coordination Pt and Ni atoms and the facile redeposition of dissolved Pt cations (not of dissolved Ni cations), resulting in the formation of a Pt-skeleton structure. After the break-in, 3 characterization CVs (Step 2) at 5 mV s^{-1} were measured to get potential-resolved dissolution signals for Pt and Ni (**Figure 1c**). Subsequently, a one-hour long AST (Step 3) composed of square-wave potential steps between 0.6 and 1.0 V (3 s at each potential) was conducted in an argon (Ar)-saturated electrolyte, following the recommendations of the Japanese FCCJ [64]. The Pt and Ni concentration signals during the AST are displayed in **Figure 1d**. Despite recording the metal dissolution signal every 0.4 seconds, the hydrodynamic conditions were insufficient to obtain time-resolved Pt and Ni dissolution signals. Finally, the break-in and the characterization CVs were reproduced after the AST (Step 4 and Step 5) to determine whether the Pt and Ni dissolution signals were stabilized. Importantly, the potential of the working electrode was kept constant at 0.4 V for 500 s between the different steps of the electrochemical aging protocol to recover stable Pt and Ni dissolution signals.

2. Qualitative insights on Pt and Ni dissolution mechanism from break-in and characterization cyclic voltammograms

Figure 2b and **Figure 2c** display the characterization CVs recorded on the Pt/C and PtNi/C catalysts during Step 2. Three independent measurements were performed for each catalyst, and the data displayed in **Figure 2b** and **Figure 2c** are representative of the average values. To allow a direct comparison of the dissolution patterns, the amounts of dissolved Pt and Ni were normalized to the intensity of the anodic peak of the third CV of Step 2 (see black arrows in **Figure 2b** and **Figure 2c**). Because the catalysts have different specific surface area, the ECSA-normalized Pt and Ni dissolution signals recorded during the third characterization CV of Step 2 are displayed in **Supplementary Figure 4**.

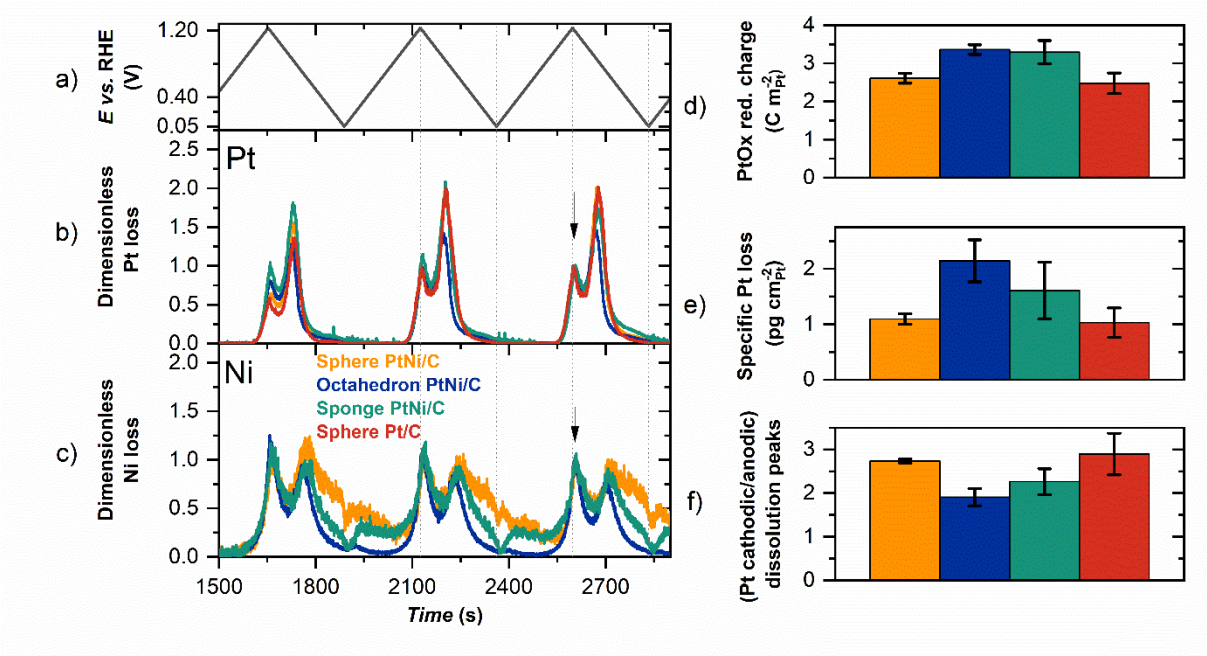

Figure 2. Dissolution of Pt and Ni from PtNi/C nanoparticles during the characterization CVs (Step 2). a) Potential profile applied at the working electrode. b) and c) display the dimensionless Pt and Ni dissolution signals during Step 2. d) Total mass of Pt lost during Step 2 normalized by ECSA. e) Electrical charge for Pt oxide reduction during a 20 mV s^{-1} CV. The values are normalized by ECSA. f)

Ratio of cathodic and anodic Pt dissolution peaks during the last cycle of Step 2. The error bars correspond to the standard deviations from three independent measurements.

In agreement with former findings, [40, 57, 61] we observed that Pt dissolution initiates at potential > 1.0 V during the anodic potential sweep independently of the presence/absence of Ni in the catalyst and of its morphology (**Figure 2b**). During the cathodic potential sweep, the Pt concentration signal first decreased down to 1.02-1.03 V before sharply increasing, largely exceeding the Pt concentration monitored during the anodic potential sweep. In line with what was discussed in the introduction, the presence of a cathodic dissolution peak is evidence that Pt and O atoms have swapped their place (place-exchange) during the 5 mV s^{-1} characterization CVs (Step 2). Importantly, higher Pt concentration monitored during the cathodic sweep does not indicate that cathodic Pt dissolution is the dominant degradation mechanism at a PEMFC cathode. Indeed, crystallite migration and corrosion of the carbon matrix [34, 65-68] also contribute to the degradation of PEMFC cathode materials, and the relative contributions of the various degradation mechanisms depend on the potential range investigated, but also on the nature of the gas atmosphere and on the temperature [58, 66, 69, 70].

Figure 2b also shows that the intensity of the Pt dissolution signal during the cathodic sweep progressively vanishes after a maximum between 0.81 and 0.86 V. This is evidence that a fraction of the dissolved Pt^{z+} ions redeposited onto the Pt/C or PtNi/C nanoparticles, leading to the formation of a Pt-rich shell covering the mother Pt-alloy core, in line with former literature findings [29, 34]. In contrast, the vast majority of the dissolved Ni cations did not redeposit during the cathodic potential sweep [71] but was progressively flushed away by the electrolyte flow. The marked decrease of the Ni dissolution signal near the LPL (E < 0.1 V) is ascribed to underpotential-deposition of Ni atoms onto the Pt-rich shell [72, 73]. The formation of a Pt-rich shell onto all PtNi/C catalysts is also supported by the shape, the position and the intensity of the Pt and Ni dissolution peaks displayed in **Figure 2b** and **Figure 2c**. Indeed, Pt and Ni atoms dissolve simultaneously in the anodic potential sweep but the cathodic Pt and Ni dissolution peaks are time and thus potential-shifted (Ni dissolution proceeding after Pt dissolution).

We now seek at identifying which nanoparticle morphology best retains Pt atoms, a critical factor influencing the long-term performance and durability of PEMFC devices. Using the third CV of Step 2 to quantify the Pt specific losses, Octahedron PtNi/C and Sponge PtNi/C appear less durable than Sphere Pt/C and Sphere PtNi/C (**Figure 2d**). Interestingly, the Pt/C and PtNi/C catalysts rank in the same order if the PtO_x reduction charge of the third CV of Step 2 is integrated (**Figure 2e**): this confirms that the place-exchange process predominantly contributes to the Pt losses when UPL = 1.23 V. As can be seen from the ratio between the integrated areas of the cathodic and anodic Pt dissolution peaks, which varies as Octahedron PtNi/C < Sponge PtNi/C < Sphere PtNi/C (**Figure 2f**), the larger quantity of Pt^{z+} ions released in the electrolyte for Octahedron PtNi/C and Sponge PtNi/C positively shifts the Pt/Pt^{z+} equilibrium potential, and facilitates the redeposition of Pt^{z+} ions (Nernst equation). Accordingly, the Ni dissolution signal in the cathodic sweep vanishes more rapidly for Octahedron PtNi/C compared to Sponge PtNi/C and Sphere PtNi/C (**Figure 2c**). Because the ability to retain Ni atoms is key to sustainable ORR activity, this result would suggest that Octahedron PtNi/C represents a wiser choice than Sponge PtNi/C and Sphere PtNi/C. However, as we will see in the next section, drawing conclusions regarding the long-term stability of bimetallic nanocatalysts cannot be derived from a simple CV. It necessitates stabilized Pt and Ni dissolution rates, which are only accessible after a prolonged AST.

3. Quantitative insights on Pt and Ni dissolution rates from square-wave potential step experiments

The Pt and Ni dissolution signals recorded during each step of the electrochemical aging protocol are represented in **Figure 3a** and **Figure 3b**. Note that the metal concentrations were normalized by the ECSA obtained from CO_{ads} stripping measurements (displayed in **Supplementary Figure 5**) or normalized by the initial Pt or Ni mass (**Supplementary Figure 6**). This normalization was performed to account for differences in crystallite/particle size among different PtNi/C catalysts. It is also important to note that a logarithmic scale was employed to encompass the wide range of elemental concentrations monitored throughout various stages of the aging protocol, including break-in, characterization, and

AST. **Figure 3c** and **Figure 3d** display the cumulated masses of Pt and Ni lost during each step and the Pt:Ni atomic ratio of the dissolved metal species is shown in **Figure 3e**.

A striking result from **Figure 3a** and **Figure 3b** is that the Pt and Ni dissolution profiles are similar for all studied PtNi/C catalysts (Sphere, Octahedron, Sponge). This indicates that the Pt and Ni dissolution mechanisms are independent of the morphology of the PtNi/C nanocatalysts. **Figure 3a** also illustrates that the concentration of dissolved Pt and Ni atoms depends on the potential variation mode and on the potential sweep rate. For example, the Pt and Ni concentrations in solution during the AST (square-wave potential sweeps between 0.6 and 1.0 V, 3 s at each potential) are one order of magnitude lower than those measured during the break-in protocol (Step 1, fast linear potential sweeps between 0.05 and 1.23 V). This is no surprise in view of the high UPL/low LPL and the fast potential sweep rate used during the break-in procedure relative to the AST, and their pronounced influence on the Pt and Ni dissolution kinetics [38, 43].

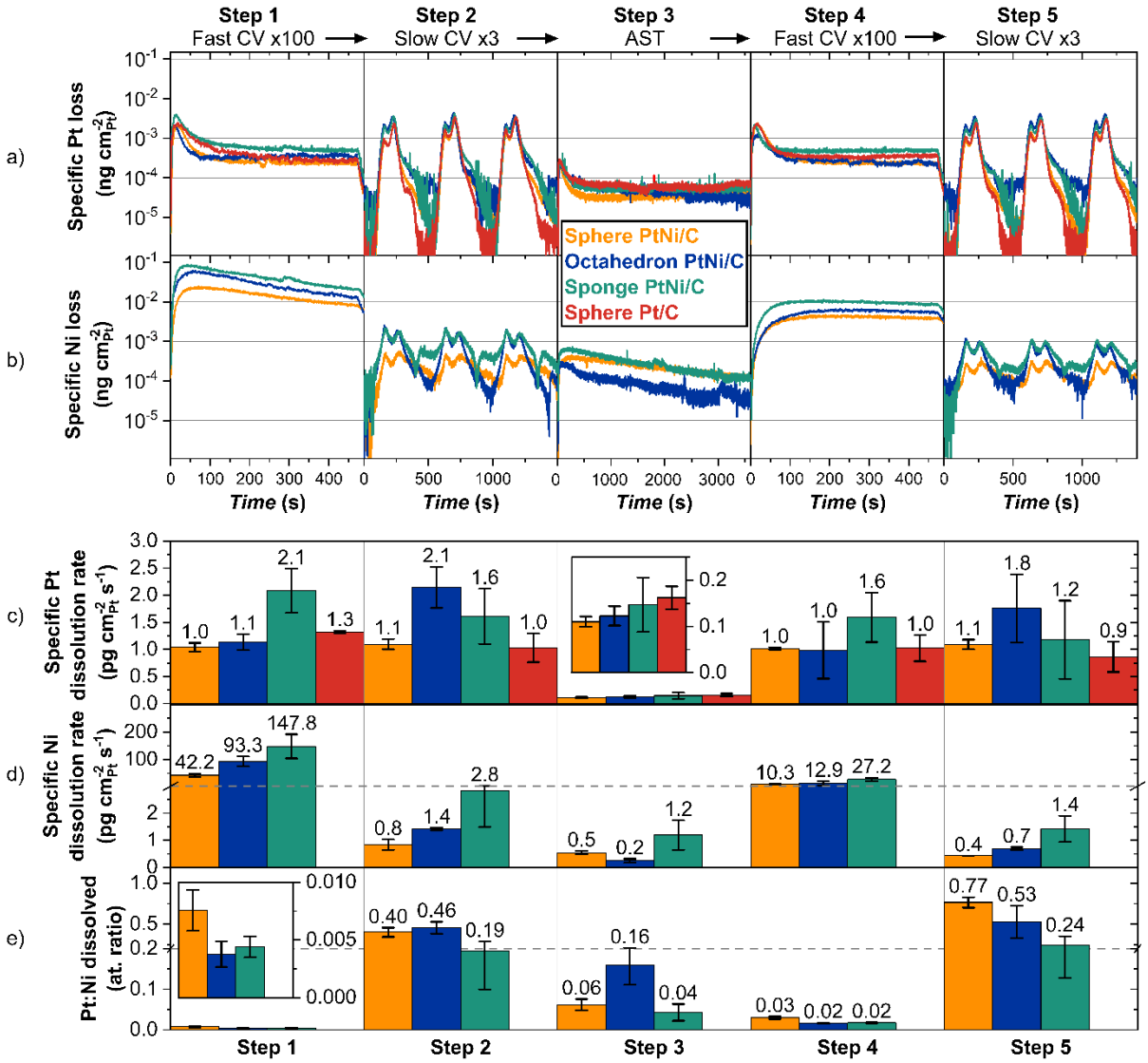

Figure 3. Pt and Ni dissolution signals during the electrochemical aging protocol. a) Pt and b) Ni dissolution signals normalized by ECSA. Scales are logarithmic to allow comparison between the different steps of the aging protocol. c) Pt and d) Ni cumulated losses during each step normalized by ECSA with corresponding error bars. e) Pt:Ni atomic ratio detected during each step with insert to highlight the low Pt:Ni ratio obtained during Step 1. The dashed gray lines represent a break in the scale. Between each step, a potential of 0.4 V is imposed to retrieve a constant Pt and Ni dissolution baseline. The error bars correspond to the standard deviations from three independent measurements.

Another important result emerges from **Figure 3a**: the Pt dissolution signals during Step 1 and Step 4 reach a plateau after *ca*. 150 s for Pt/C and all PtNi/C catalysts, confirming a morphology-independent Pt dissolution mechanism. In contrast, the Ni dissolution profiles were consistent among all PtNi/C

catalysts during Step 1 and Step 4 but a steady Ni dissolution signal was only reached after the AST, *i.e.* during Step 4. This suggests that a harsh break-in and a long AST are required to measure steady-state metal dissolution rates with a FC-ICP-MS set-up.

Quantitively speaking, we observed nearly a two-order-of-magnitude difference in the dissolution rates between Pt and Ni under the highly dynamic conditions of the break-in steps (Step 1 and Step 4), see **Figure 3a** and **Figure 3b**. This large difference results from the propensity of Pt^{z+} ions to electrochemically redeposit, unlike Ni^{2+} ions. Further supporting this statement is the sweep rate independence of the Pt dissolution rate, which is not the case for the Ni dissolution rate (the potential sweep rate is 500/5 mV s^{-1} for Step 1/4 and Step 2/5, respectively in **Figure 3c** and **Figure 3d**). Consequently, the Pt:Ni atomic ratio in the electrolyte was 5 times (Step 2 and Step 5) to 50 times (Step 1, Step 3 and Step 4) lower than the nominal composition of the pristine PtNi/C catalysts (estimated from ICP-MS analyses on digested PtNi/C powders, see **Supplementary Table 1**). Moreover, as the Pt dissolution rate remained nearly constant while the Ni dissolution rate decreased over time (**Figure 3d**), the Pt:Ni atomic ratio in the electrolyte steadily increased (**Figure 3e**). These results confirm former conclusions from aged PEMFC cathodes [30-34, 74-76] that transition metal atoms are continuously leaching out from Pt-alloy/C catalysts. They also support our former conclusion that short-duration AST or CVs cannot be used to quantitatively predict the resistance to dissolution of bimetallic nanocatalysts. In the one-hour AST conditions of Step 3 reflecting the potential range experienced by PtNi/C catalysts at a PEMFC cathode (excursions to potentials exceeding 1 V are unlikely to happen instead during unprotected start-up/shutdown events [77]), Octahedron PtNi/C best retain Pt and Ni atoms during model PEMFC operating conditions (**Figure 3** and **Supplementary Figure 6**). Now, should the UPL exceed 1 V (*e.g.* during characterization CVs) or should the complete electrochemical aging protocol be considered, Sphere PtNi/C provides the best stability compromise (**Supplementary Figure 7**).

Summing up, we have shown in this section that stabilized Pt and Ni dissolution rates can be obtained, provided that experimental FC-ICP-MS conditions (harsh break-in protocol, long AST) are properly chosen. From the 2-hour electrochemical aging protocol used in this study, we show that the nanocatalyst's morphology affects the Pt and Ni dissolution rate, not their dissolution mechanisms.

We also report that Ni atoms are continuously leached out from PtNi/C catalysts. Knowing the deleterious effects of transition metal cations on proton conductivity, [78-80] water uptake [81, 82] and mechanical toughness [83] of ionomer/ membrane, the question then arises whether *ex situ* chemical leaching can attenuate or even prevent the dissolution of Ni atoms in model PEMFC cathode conditions.

4. Effect of *ex situ* formation of Pt-skeleton on Pt and Ni losses

As Sphere PtNi/C was identified as the most stable catalyst during the full aging protocol, a given mass of this nanocatalyst was acid-treated for 24 h in 1 M H_2SO_4 at room temperature under air (open-circuit potential close to 1.0 V). The acid-treated commercial PtNi/C sample is referred to as Sphere PtNi/C-AT. As shown by **Supplementary Table 1**, acid-leaching leads to an increase of the Pt:Ni atomic ratio in the catalyst (from 3.2 to 4.6 for Sphere PtNi/C and Sphere PtNi/C-AT, respectively *i.e.* 30 % of Ni atoms were removed by the acid-leaching process) but does not change its lattice parameter. As 30 % of the atoms are surface atoms on a 5 nm PtNi nanoparticle, [84] the monitored 30 % reduction in Ni content implies formation of a Pt-rich shell approximately 1-2 monolayers thick on Sphere PtNi/C-AT. This observation is in good agreement with former measurements on acid-treated Pt_3Co/C or Pt_3Ni/C nanoparticles using spot-resolved energy-dispersive spectroscopy, [74, 85] Synchrotron X-ray diffraction [32] or electron energy loss spectroscopy [29]. Similar CVs and ORR activities measured on the Sphere PtNi/C-AT and Sphere PtNi/C (**Supplementary Figure 8**) indicate that the loss of Ni from the outermost surface layers does not affect their ORR activity, in line with earlier findings [29, 85].

The Pt and Ni dissolution signals recorded on Sphere PtNi/C and Sphere PtNi/C-AT during Step 1 and Step 4 (break-in steps) are displayed in **Figure 4a** and **Figure 4b**. The dissolution signals are homothetic, pointing towards identical Pt and Ni dissolution mechanisms for Sphere PtNi/C and Sphere PtNi/C-AT. Quantitatively speaking, the ECSA-normalized Pt loss is slightly increased for Sphere PtNi/C-AT relative to Sphere PtNi/C during Step 1 (**Figure 4c**), which could be due to the higher proportion of under coordinated Pt atoms of the former. Interestingly, the difference in specific Pt loss between the two materials persists during Step 4, that is after the one-hour long AST (Step 3). In contrast,

a 47 % decrease of the ECSA-normalized Ni loss is reported for PtNi/C-AT compared to Sphere PtNi/C during Step 1. Similar trend during Step 4 (42 % decrease of ECSA-normalized Ni losses) suggests that the presence of the Pt-rich shell attenuates the Ni dissolution rate. The benefit arising from acid-leaching is also obvious when one compares the bulk Pt:Ni atomic ratio in the pristine Sphere PtNi/C and Sphere PtNi/C-AT catalysts and the Pt:Ni ratio in the electrolyte (**Figure 4d**). We therefore conclude that acid-leaching is an effective strategy for reducing the overall amount of dissolved Ni in the electrolyte and mitigating the degradation of mass transport properties in the ionomer/membrane associated with the partial exchange of protons by Ni cations, while maintaining high beginning of life ORR activity (**Supplementary Figure 8**).

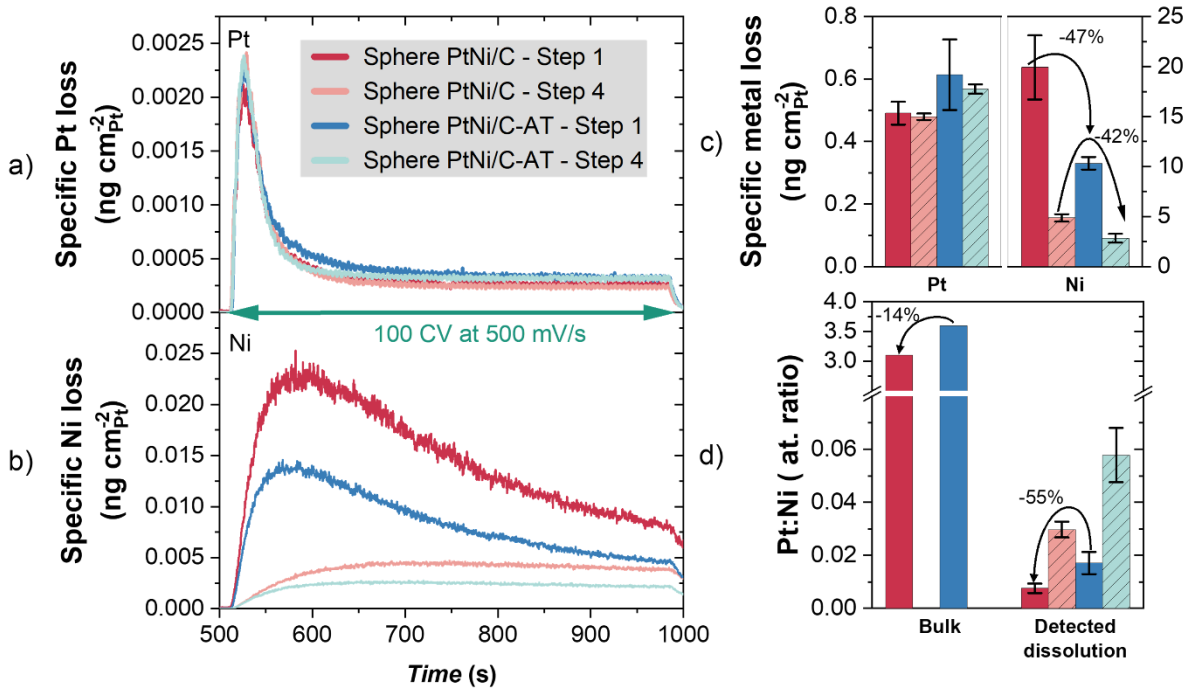

Figure 4. Effect of acid leaching on Pt and Ni dissolution rates. a) Pt and b) Ni are ECSA-normalized dissolution signals for the pristine PtNi/C Sphere and acid-leached PtNi/C Sphere catalysts during Step 1 and Step 4, c) displays ECSA-normalized Pt and Ni cumulated losses during Step 1 and Step 4, d) compares the Pt:Ni atomic ratio in the pristine Sphere PtNi/C and Sphere PtNi/C-AT catalysts and dissolved in the electrolyte during Step 1 and Step 4. The error bars correspond to the standard deviations from three independent measurements.

CONCLUSIONS

In summary, using an electrochemical flow cell coupled to inductively-coupled plasma mass spectrometry, we have investigated the dissolution mechanism of spherical, octahedral and spongy PtNi/C nanocatalysts, when subjected to linear ramp or square-wave potential ramp experiments. Morphology-independent Pt and Ni dissolution profiles were measured for the three PtNi/C catalysts, as a result of the formation of a Pt-rich shell covering the underlying PtNi core, so called Pt-skeleton nanostructure. The Pt-skeleton nanostructure reduces the dissolution of Ni atoms in all PtNi/C catalysts, as long as the cathode potential remains below 1.0 V. Exposure to higher potentials, such as those experienced during start-stop events, results in simultaneous dissolution of both Pt and Ni. The FC-ICP-MS results also suggest that *ex situ* acid leaching mitigates the overall loss of Ni atoms during the AST, but it does not alter the dissolution mechanism of Pt and Ni. From a methodological point of view, our study indicates that steady-state Pt and Ni dissolution rates can be obtained using harsh break-in conditions and long AST. This methodological outcome is of crucial importance since it could circumvent difficulties in predicting the lifetime of electrocatalysts using FC-ICP-MS. Focusing solely on the impact of nanoparticle shape on the retention of Pt and Ni, we observe that the least oxyphilic catalyst (Sphere PtNi/C) demonstrates superior retention of Pt and Ni atoms.

CRediT authorship contribution statement

Camille Roiron: Nanocatalysts synthesis, Sample collection and analysis; Methodology, Investigation; Formal analysis; Drawing; Data curation; Writing – original draft. **Vincent Martin**: Sample collection and analysis; Investigation; Data curation. **Kavita Kumar**: Sample collection and analysis; Investigation. **Laetitia Dubau**: Conceptualization, Data curation; Funding acquisition; Methodology, Project administration; Resources; Supervision; Validation. **Frédéric Maillard**: Conceptualization; Data curation; Funding acquisition; Methodology; Resources; Supervision; Validation; Writing – review & editing.

Declaration of competing interest

The authors declare that they have no known competing financial interests or personal relationships that could have appeared to influence the work reported in this paper.

Appendix A. Supporting information

Supplementary data associated with this article can be found in the online version at DOI.

ACKNOWLEDGMENTS

This work was supported by the French National Research Agency via the BRIDGE project (grant number ANR-19-ENER-0008-01).

REFERENCES

[1] K.C. Neyerlin, W. Gu, J. Jorne, H.A. Gasteiger, Determination of catalyst unique parameters for the oxygen reduction reaction in a PEMFC, J. Electrochem. Soc., 153 (2006) A1955-A1963.

[2] V.R. Stamenkovic, B.S. Mun, M. Arenz, K.J.J. Mayrhofer, C.A. Lucas, G.F. Wang, P.N. Ross, N.M. Markovic, Trends in electrocatalysis on extended and nanoscale Pt-bimetallic alloy surfaces, Nature Mater., 6 (2007) 241-247.

[3] J. Greeley, I.E.L. Stephens, A.S. Bondarenko, T.P. Johansson, H.A. Hansen, T.F. Jaramillo, J. Rossmeisl, I. Chorkendorff, J.K. Nørskov, Alloys of platinum and early transition metals as oxygen reduction electrocatalysts, Nat. Chem., 1 (2009) 552-556.

[4] M. Escudero-Escribano, P. Malacrida, M.H. Hansen, U.G. Vej-Hansen, A. Velázquez-Palenzuela, V. Tripkovic, J. Schiøtz, J. Rossmeisl, I.E.L. Stephens, I. Chorkendorff, Tuning the activity of Pt alloy electrocatalysts by means of the lanthanide contraction, Science, 352 (2016) 73-76.

[5] T. Asset, R. Chattot, M. Fontana, B. Mercier-Guyon, N. Job, L. Dubau, F. Maillard, A review on recent developments and prospects for the oxygen reduction reaction on hollow Pt-alloy nanoparticles, Chemphyschem, 19 (2018) 1552-1567.

[6] L. Pan, S. Ott, F. Dionigi, P. Strasser, Current challenges related to the deployment of shape-controlled Pt alloy oxygen reduction reaction nanocatalysts into low Pt-loaded cathode layers of proton exchange membrane fuel cells, Curr. Opin. Electrochem., 18 (2019) 61-71.

[7] J.R. Kitchin, J.K. Norskov, M.A. Barteau, J.G. Chen, Role of strain and ligand effects in the modification of the electronic and chemical properties of bimetallic surfaces, Phys Rev Lett, 93 (2004) 156801.

[8] V. Stamenkovic, B.S. Mun, K.J. Mayrhofer, P.N. Ross, N.M. Markovic, J. Rossmeisl, J. Greeley, J.K. Norskov, Changing the activity of electrocatalysts for oxygen reduction by tuning the surface electronic structure, Angew. Chem. Int. Ed., 45 (2006) 2897-2901.

[9] V.R. Stamenkovic, B. Fowler, B.S. Mun, G.F. Wang, P.N. Ross, C.A. Lucas, N.M. Markovic, Improved oxygen reduction activity on $Pt_3Ni(111)$ via increased surface site availability, Science, 315 (2007) 493-497.

[10] F. Elkadiri, R. Faure, R. Durand, Electrochemical reduction of molecular-oxygen on platinum single-crystals, J. Electroanal. Chem., 301 (1991) 177-188.

[11] N.M. Markovic, H.A. Gasteiger, P.N. Ross, Oxygen reduction on platinum low-index single crystal surfaces in sulfuric acid-solution - Rotating ring-Pt(hkl) disk studies, J. Phys. Chem., 99 (1995) 3411-3415.

[12] C. Cui, L. Gan, M. Heggen, S. Rudi, P. Strasser, Compositional segregation in shaped Pt alloy nanoparticles and their structural behaviour during electrocatalysis, Nature Mater., 12 (2013) 765-771.

[13] R. Chattot, O. Le Bacq, V. Beermann, S. Kühl, J. Herranz, S. Henning, L. Kühn, T. Asset, L. Guétaz, G. Renou, J. Drnec, P. Bordet, A. Pasturel, A. Eychmüller, T.J. Schmidt, P. Strasser, L. Dubau, F. Maillard, Surface distortion as a unifying concept and descriptor in oxygen reduction reaction electrocatalysis, Nature Mater., 17 (2018) 827-833.

[14] L. Dubau, T. Asset, R. Chattot, C. Bonnaud, V. Vanpeene, J. Nelayah, F. Maillard, Tuning the performance and the stability of porous hollow PtNi/C nanostructures for the oxygen reduction reaction, ACS Catal., 5 (2015) 5333-5341.

[15] L. Dubau, J. Nelayah, S. Moldovan, O. Ersen, P. Bordet, J. Drnec, T. Asset, R. Chattot, F. Maillard, Defects do catalysis: CO monolayer oxidation and oxygen reduction reaction on hollow PtNi/C nanoparticles, ACS Catal., 6 (2016) 4673-4684.

[16] M.F. Li, Z.P. Zhao, T. Cheng, A. Fortunelli, C.Y. Chen, R. Yu, Q.H. Zhang, L. Gu, B.V. Merinov, Z.Y. Lin, E.B. Zhu, T. Yu, Q.Y. Jia, J.H. Guo, L. Zhang, W.A. Goddard, Y. Huang, X.F. Duan, Ultrafine jagged platinum nanowires enable ultrahigh mass activity for the oxygen reduction reaction, Science, 354 (2016) 1414-1419.

[17] S. Henning, L. Kuhn, J. Herranz, J. Durst, T. Binninger, M. Nachtegaal, M. Werheid, W. Liu, M. Adam, S. Kaskel, A. Eychmuller, T.J. Schmidt, Pt-Ni aerogels as unsupported electrocatalysts for the oxygen reduction reaction, J. Electrochem. Soc., 163 (2016) F998-F1003.

[18] S. Henning, H. Ishikawa, L. Kuhn, J. Herranz, E. Muller, A. Eychmuller, T.J. Schmidt, Unsupported Pt-Ni aerogels with enhanced high current performance and durability in fuel cell cathodes, Angew. Chem. Int. Ed., 56 (2017) 10707-10710.

[19] R. Chattot, T. Asset, P. Bordet, J. Drnec, L. Dubau, F. Maillard, Beyond strain and ligand effects: Microstrain-induced enhancement of the oxygen reduction reaction kinetics on various PtNi/C nanostructures, ACS Catal., 7 (2017) 398-408.

[20] L. Dubau, J. Nelayah, T. Asset, R. Chattot, F. Maillard, Implementing structural disorder as a promising direction for improving the stability of PtNi/C nanoparticles, ACS Catal., 7 (2017) 3072-3081.

[21] R. Chattot, P. Bordet, I. Martens, J. Drnec, L. Dubau, F. Maillard, Building practical descriptors for defect engineering of electrocatalytic materials, ACS Catal., 10 (2020) 9046-9056.

[22] O. Le Bacq, A. Pasturel, R. Chattot, B. Previdello, J. Nelayah, T. Asset, L. Dubau, F. Maillard, Effect of atomic vacancies on the structure and the electrocatalytic activity of Pt-rich/C nanoparticles: A combined experimental and density functional theory study, ChemCatChem, 9 (2017) 2324-2338.

[23] R. Chattot, I. Martens, M. Scohy, J. Herranz, J. Drnec, F. Maillard, L. Dubau, Disclosing Pt-bimetallic alloy nanoparticle surface lattice distortion with electrochemical probes, ACS Energy Lett., 5 (2020) 162-169.

[24] T. Toda, H. Igarashi, M. Watanabe, Role of electronic property of Pt and Pt alloys on electrocatalytic reduction of oxygen, J. Electrochem. Soc., 145 (1998) 4185-4188.

[25] T. Toda, H. Igarashi, H. Uchida, M. Watanabe, Enhancement of the electroreduction of oxygen on Pt alloys with Fe, Ni, and Co, J. Electrochem. Soc., 146 (1999) 3750-3756.

[26] L.J. Wan, T. Moriyama, M. Ito, H. Uchida, M. Watanabe, *In situ* STM imaging of surface dissolution and rearrangement of a Pt-Fe alloy electrocatalyst in electrolyte solution, Chem. Commun., (2002) 58-59.

[27] S.C. Zignani, E. Antolini, E.R. Gonzalez, Evaluation of the stability and durability of Pt and Pt-Co/C catalysts for polymer electrolyte membrane fuel cells, J. Power Sources, 182 (2008) 83-90.

[28] S. Chen, W.C. Sheng, N. Yabuuchi, P.J. Ferreira, L.F. Allard, Y. Shao-Horn, Origin of oxygen reduction reaction activity on "Pt_3Co" nanoparticles: Atomically resolved chemical compositions and structures, J. Phys. Chem. C, 113 (2009) 1109-1125.

[29] J. Durst, M. Lopez-Haro, L. Dubau, M. Chatenet, Y. Soldo-Olivier, L. Guétaz, P. Bayle-Guillemaud, F. Maillard, Reversibility of Pt-skin and Pt-skeleton nanostructures in acidic media, J. Phys. Chem. Lett., 5 (2014) 434-439.

[30] L. Dubau, F. Maillard, M. Chatenet, J. André, E. Rossinot, Nanoscale compositional changes and modification of the surface reactivity of Pt_3Co/C nanoparticles during proton-exchange membrane fuel cell operation, Electrochim. Acta, 56 (2010) 776-783.

[31] L. Dubau, F. Maillard, M. Chatenet, L. Guétaz, J. André, E. Rossinot, Durability of Pt_3Co/C cathodes in a 16 cell PEMFC stack: Macro/microstructural changes and degradation mechanisms, J. Electrochem. Soc., 157 (2010) B1887-B1895.

[32] F. Maillard, L. Dubau, J. Durst, M. Chatenet, J. André, E. Rossinot, Durability of Pt_3Co/C nanoparticles in a proton-exchange membrane fuel cell: Direct evidence of bulk Co segregation to the surface, Electrochem. Commun., 12 (2010) 1161-1164.

[33] L. Dubau, J. Durst, F. Maillard, L. Guétaz, M. Chatenet, J. André, E. Rossinot, Further insights into the durability of Pt_3Co/C electrocatalysts: formation of Pt hollow nanoparticles induced by the Kirkendall effect, Electrochim. Acta, 56 (2011) 10658-10667.

[34] L. Dubau, M. Lopez-Haro, L. Castanheira, J. Durst, M. Chatenet, P. Bayle-Guillemaud, L. Guétaz, N. Caqué, E. Rossinot, F. Maillard, Probing the structure, the composition and the ORR activity of Pt_3Co/C nanocrystallites during a 3422 h PEMFC ageing test, Appl. Catal., B, 142-143 (2013) 801-808.

[35] M. Lopez-Haro, L. Dubau, L. Guétaz, P. Bayle-Guillemaud, M. Chatenet, J. André, N. Caqué, E. Rossinot, F. Maillard, Atomic-scale structure and composition of Pt_3Co/C nanocrystallites during real PEMFC operation: A STEM–EELS study, Appl. Catal., B, 152-153 (2014) 300-308.

[36] V.R. Stamenkovic, B.S. Mun, K.J. Mayrhofer, P.N. Ross, N.M. Markovic, Effect of surface composition on electronic structure, stability, and electrocatalytic properties of Pt-transition metal alloys: Pt-skin versus Pt-skeleton surfaces, J. Am. Chem. Soc., 128 (2006) 8813-8819.

[37] S.O. Klemm, A.A. Topalov, C.A. Laska, K.J.J. Mayrhofer, Coupling of a high throughput microelectrochemical cell with online multielemental trace analysis by ICP-MS, Electrochem. Com., 13 (2011) 1533-1535.

[38] J.C. Meier, C. Galeano, I. Katsounaros, J. Witte, H.J. Bongard, A.A. Topalov, C. Baldizzone, S. Mezzavilla, F. Schüth, K.J.J. Mayrhofer, Design criteria for stable Pt/C fuel cell catalysts, Beilstein J. Nanotechnol., 5 (2014) 44-67.

[39] P. Jovanovič, A. Pavlišič, V.S. Šelih, M. Šala, N. Hodnik, M. Bele, S. Hočevar, M. Gaberšček, New insight into platinum dissolution from nanoparticulate platinum-based electrocatalysts using highly sensitive *in situ* concentration measurements, ChemCatChem, 6 (2014) 449-453.

[40] R.K. Ahluwalia, D.D. Papadias, N.N. Kariuki, J.K. Peng, X. Wang, Y. Tsai, D.G. Graczyk, D.J. Myers, Potential dependence of Pt and Co dissolution from platinum-cobalt alloy PEFC catalysts using time-resolved measurements, J. Electrochem. Soc., 165 (2018) F3024-F3035.

[41] O. Kasian, S. Geiger, K.J.J. Mayrhofer, S. Cherevko, Electrochemical on-line ICP-MS in electrocatalysis research, Chem. Rec., 19 (2019) 2130-2142.

[42] S. Abbou, R. Chattot, V. Martin, F. Claudel, L. Solà-Hernandez, C. Beauger, L. Dubau, F. Maillard, Manipulating the corrosion resistance of SnO_2 aerogels through doping for efficient and durable oxygen evolution reaction electrocatalysis in acidic media, ACS Catal., 10 (2020) 7283–7294.

[43] A.A. Topalov, I. Katsounaros, M. Auinger, S. Cherevko, J.C. Meier, S.O. Klemm, K.J.J. Mayrhofer, Dissolution of platinum: Limits for the deployment of electrochemical energy conversion?, Angew. Chem. Int. Ed., 51 (2012) 12613-12615.

[44] S. Cherevko, G.P. Keeley, S. Geiger, A.R. Zeradjanin, N. Hodnik, N. Kulyk, K.J.J. Mayrhofer, Dissolution of platinum in the operational range of fuel cells, ChemElectroChem, 2 (2015) 1471-1478.

[45] S. Cherevko, A.R. Zeradjanin, G.P. Keeley, K.J.J. Mayrhofer, A comparative study on gold and platinum dissolution in acidic and alkaline media, J. Electrochem. Soc., 161 (2014) H822-H830.

[46] A. Pavlišič, P. Jovanovič, V.S. Šelih, M. Šala, N. Hodnik, M. Gaberšček, Platinum dissolution and redeposition from Pt/C fuel cell electrocatalyst at potential cycling, J. Electrochem. Soc., 165 (2018) F3161.

[47] F.D. Speck, A. Zagalskaya, V. Alexandrov, S. Cherevko, Periodicity in the electrochemical dissolution of transition metals, Angew. Chem. Int. Ed., 60 (2021) 13343-13349.

[48] M.A.H. Lanyon, B.M.W. Trapnell, C.N. Hinshelwood, The interaction of oxygen with clean metal surfaces, Proceedings of the Royal Society of London. Series A. Mathematical and Physical Sciences, 227 (1955) 387-399.

[49] N. Sato, The kinetics of anodic oxidation of iron in neutral solution: I. Steady growth region, J. Electrochem. Soc., 111 (1964) 512-519.

[50] B.E. Conway, Electrochemical oxide film formation at noble metals as a surface-chemical process, Prog. Surf. Sci., 49 (1995) 331-452.

[51] Z. Nagy, H. You, Applications of surface X-ray scattering to electrochemistry problems, Electrochim. Acta, 47 (2002) 3037-3055.

[52] G. Jerkiewicz, G. Vatankhah, J. Lessard, M.P. Soriaga, Y.S. Park, Surface-oxide growth at platinum electrodes in aqueous H_2SO_4 Reexamination of its mechanism through combined cyclic-voltammetry, electrochemical quartz-crystal nanobalance, and Auger electron spectroscopy measurements, Electrochim. Acta, 49 (2004) 1451-1459.

[53] S. Cherevko, A.A. Topalov, A.R. Zeradjanin, G.P. Keeley, K.J.J. Mayrhofer, Temperature-dependent dissolution of polycrystalline platinum in sulfuric acid electrolyte, Electrocatalysis, 5 (2014) 235-240.

[54] T. Fuchs, J. Drnec, F. Calle-Vallejo, N. Stubb, D.J.S. Sandbeck, M. Ruge, S. Cherevko, D.A. Harrington, O.M. Magnussen, Structure dependency of the atomic-scale mechanisms of platinum electro-oxidation and dissolution, Nat. Catal., 3 (2020) 754-761.

[55] T. Fuchs, V. Briega-Martos, J. Drnec, N. Stubb, I. Martens, F. Calle-Vallejo, D.A. Harrington, S. Cherevko, O.M. Magnussen, Anodic and cathodic platinum dissolution processes involve different oxide species, Angew. Chem. Int. Ed., 62 (2023) e202304293.

[56] A.A. Topalov, S. Cherevko, A.R. Zeradjanin, J.C. Meier, I. Katsounaros, K.J.J. Mayrhofer, Towards a comprehensive understanding of platinum dissolution in acidic media, Chem. Sci., 5 (2014) 631-638.

[57] T. Đukić, L.J. Moriau, L. Pavko, M. Kostelec, M. Prokop, F. Ruiz-Zepeda, M. Šala, G. Dražić, M. Gatalo, N. Hodnik, Understanding the crucial significance of the temperature and potential window on the stability of carbon supported Pt-alloy nanoparticles as oxygen reduction reaction electrocatalysts, ACS Catal., 12 (2022) 101-115.

[58] L. Dubau, F. Maillard, Unveiling the crucial role of temperature on the stability of oxygen reduction reaction electrocatalysts, Electrochem. Com., 63 (2016) 65-69.

[59] C. Baldizzone, L. Gan, N. Hodnik, G.P. Keeley, A. Kostka, M. Heggen, P. Strasser, K.J.J. Mayrhofer, Stability of dealloyed porous Pt/Ni nanoparticles, ACS Catal., 5 (2015) 5000-5007.

[60] M. Gatalo, P. Jovanovič, U. Petek, M. Šala, V.S. Šelih, F. Ruiz-Zepeda, M. Bele, N. Hodnik, M. Gaberščček, Comparison of Pt–Cu/C with benchmark Pt–Co/C: Metal dissolution and their surface interactions, ACS Appl. Energy Mater., 2 (2019) 3131-3141.

[61] L.J. Moriau, A. Hrnjić, A. Pavlišič, A.R. Kamšek, U. Petek, F. Ruiz-Zepeda, M. Šala, L. Pavko, V.S. Šelih, M. Bele, P. Jovanovič, M. Gatalo, N. Hodnik, Resolving the nanoparticles' structure-property relationships at the atomic level: a study of Pt-based electrocatalysts, iScience, 24 (2021).

[62] X. Huang, Z. Zhao, Y. Chen, E. Zhu, M. Li, X. Duan, Y. Huang, A rational design of carbon-supported dispersive Pt-based octahedra as efficient oxygen reduction reaction catalysts, Energy Environ. Sci., 7 (2014) 2957-2962.

[63] R. Chattot, C. Roiron, K. Kumar, V. Martin, C.A. Campos Roldan, M. Mirolo, I. Martens, L. Castanheira, A. Viola, R. Bacabe, S. Cavaliere, P.Y. Blanchard, L. Dubau, F. Maillard, J. Drnec, Break-in bad: On the conditioning of fuel cell nanoalloy catalysts, ACS Catal., 12 (2022) 15675-15685.

[64] A. Ohma, K. Shinohara, A. Iiyama, T. Yoshida, A. Daimaru, Membrane and catalyst performance targets for automotive fuel cells by FCCJ membrane, catalyst, MEA WG, ECS Trans., 41 (2011) 775-784.

[65] Z. Zhao, L. Dubau, F. Maillard, Evidences of the migration of Pt crystallites on high surface area carbon supports in the presence of reducing molecules, J. Power Sources, 217 (2012) 449-458.

[66] L. Dubau, L. Castanheira, G. Berthomé, F. Maillard, An identical-location transmission electron microscopy study on the degradation of Pt/C nanoparticles under oxidizing, reducing and neutral atmosphere, Electrochim. Acta, 110 (2013) 273-281.

[67] L. Castanheira, L. Dubau, M. Mermoux, G. Berthomé, N. Caqué, E. Rossinot, M. Chatenet, F. Maillard, Carbon corrosion in proton-exchange membrane fuel cells: From model experiments to real-life operation in membrane electrode assemblies, ACS Catal., 4 (2014) 2258-2267.

[68] L. Castanheira, W.O. Silva, F.H.B. Lima, A. Crisci, L. Dubau, F. Maillard, Carbon corrosion in proton-exchange membrane fuel cells: Effect of the carbon structure, the degradation protocol, and the gas atmosphere, ACS Catal., (2015) 2184-2194.

[69] Z. Zhao, L. Castanheira, L. Dubau, G. Berthomé, A. Crisci, F. Maillard, Carbon corrosion and platinum nanoparticles ripening under open circuit potential conditions, J. Power Sources, 230 (2013) 236-243.

[70] L. Castanheira, L. Dubau, F. Maillard, Accelerated stress tests of Pt/HSAC electrocatalysts: an identical-location transmission electron microscopy study on the influence of intermediate characterizations, Electrocatalysis, 5 (2014) 125-135.

[71] M. Pourbaix, Atlas of electrochemical equilibria in aqueous solutions, National Association of Corrosion Engineers, Houston, 1979, pp. 453.

[72] M. Chatenet, R. Faure, Y. Soldo-Olivier, Nickel-underpotential deposition on Pt(110) in sulphate-containing media, J. Electroanal. Chem., 580 (2005) 275-283.

[73] F.J. Sarabia, V. Climent, J.M. Feliu, Underpotential deposition of nickel on platinum single crystal electrodes, J. Electroanal. Chem., 819 (2018) 391-400.

[74] S. Chen, H.A. Gasteiger, K. Hayakawa, T. Tada, Y. Shao-Horn, Platinum-alloy cathode catalyst degradation in proton exchange membrane fuel cells: Nanometer-ccale compositional and morphological changes, J. Electrochem. Soc., 157 (2010) A82-A97.

[75] C.E. Carlton, S. Chen, P.J. Ferreira, L.F. Allard, Y. Shao-Horn, Sub-nanometer-resolution elemental mapping of "Pt_3Co" nanoparticle catalyst degradation in proton-exchange membrane fuel cells, J. Phys. Chem. Lett., 3 (2012) 161-166.

[76] Y. Yu, H.L. Xin, R. Hovden, D. Wang, E.D. Rus, J.A. Mundy, D.A. Muller, H.D. Abruña, Three-dimensional tracking and visualization of hundreds of Pt-Co fuel cell nanocatalysts during electrochemical aging, Nano Lett., 12 (2012) 4417-4423.

[77] J. Durst, A. Lamibrac, F. Charlot, J. Dillet, L.F. Castanheira, G. Maranzana, L. Dubau, F. Maillard, M. Chatenet, O. Lottin, Degradation heterogeneities induced by repetitive start/stop events in proton exchange membrane fuel cell: Inlet *vs*. outlet and channel *vs*. land, Appl. Catal., B, 138–139 (2013) 416-426.

[78] T. Okada, Y. Ayato, M. Yuasa, I. Sekine, The effect of impurity cations on the transport characteristics of perfluorosulfonated ionomer membranes, J. Phys. Chem. B, 103 (1999) 3315-3322.

[79] M.J. Kelly, G. Fafilek, J.O. Besenhard, H. Kronberger, G.E. Nauer, Contaminant absorption and conductivity in polymer electrolyte membranes, J. Power Sources, 145 (2005) 249-252.

[80] H. Wang, J.A. Turner, The influence of metal ions on the conductivity of Nafion 112 in polymer electrolyte membrane fuel cell, J. Power Sources, 183 (2008) 576-580.

[81] G. Xie, T. Okada, T. Arimura, Fourier transform infrared spectroscopy study of fully hydrated Nafion membranes of various cation forms, Z. Phys. Chem., 205 (1998) 113-125.

[82] G. Suresh, Y. Scindia, A. Pandey, A. Goswami, Self-diffusion coefficient of water in Nafion-117 membrane with different monovalent counterions: a radiotracer study, J. Membr. Sci., 250 (2005) 39-45.

[83] R. Jia, B. Han, K. Levi, T. Hasegawa, J. Ye, R.H. Dauskardt, Effect of cation contamination and hydrated pressure loading on the mechanical properties of proton exchange membranes, J. Power Sources, 196 (2011) 3803-3809.

[84] R.E. Benfield, Mean coordination numbers and the non-metal–metal transition in clusters, J. Chem. Soc., Faraday Trans., 88 (1992) 1107 - 1110.

[85] C. Wang, M. Chi, D. Li, D. Strmcnik, D. Van Der Vliet, G. Wang, V. Komanicky, K.C. Chang, A.P. Paulikas, D. Tripkovic, J. Pearson, K.L. More, N.M. Markovic, V.R. Stamenkovic, Design and synthesis of bimetallic electrocatalyst with multilayered Pt-skin surfaces, J. Am. Chem. Soc., 133 (2011) 14396-14403.